



ELSEVIER

Contents lists available at ScienceDirect

Fuel

journal homepage: www.elsevier.com/locate/fuel

Full Length Article

Large eddy simulation of non-reacting flow and mixing fields in a rotating detonation engine

Majie Zhao, Huangwei Zhang*

Department of Mechanical Engineering, National University of Singapore, 9 Engineering Drive 1, Singapore 117576, Singapore

ARTICLE INFO

Keywords:

Rotating detonation engine
 Periodic burner sector
 Non-premixed reactant
 Turbulent mixing
 Detonability range
 Large eddy simulation

ABSTRACT

Large Eddy Simulations (LES) of the non-reacting flow and mixing fields in a Rotating Detonation Engine (RDE) from Air Force Research Laboratory (AFRL) are performed. Effects of the total number of fuel injection orifices and air flow rates on the mixing in the AFRL RDE are studied using a periodic burner sector with five injection orifices. The instantaneous vortex structures and shock wave in the non-reactive AFRL RDE are identified, and the structures are found to be similar to those in jet in crossflow. Also, the compositional non-uniformity in the height and azimuthal directions of the burner is observed. The mixing efficiency, root-mean-square value of the hydrogen mass fraction and mixing area ratios are introduced to quantify the mixing process. The observations from LES qualitatively justify the behaviors of detonation fronts observed in the experiments. Finally, results based on full scale AFRL RDE are briefly discussed.

1. Introduction

Rotating Detonation Engines (RDE) have attracted the attention from more and more researchers [1,2] in recent decades due to high efficiency of the detonation thermal cycle related to pressure gain combustion. Compared to other detonation engines, e.g. Pulsed Detonation Engines (PDE) [3], RDE can provide a steady source of thrust once ignited and scale up to larger thrust sizes easily. Also, due to the relatively small scale, they can be possibly applied in practical propulsion devices [4], e.g. turbomachinery. Therefore, RDE has the potential to become one of the next-generation propulsion systems.

The feasibility of RDE was first verified by Voitsekhoovskii [5] with premixed oxygen/acetylene mixture in a disc-shaped setup. Since that, extensive studies on RDE, including numerical simulations and experimental measurements, have been performed [2]. In an actual RDE combustion chamber, fully premixed injection is certainly the ideal implementation to obtain stable detonative combustion, but it is difficult to be realized and actively controlled. Additionally, flashback may occur when the premixed reactants are supplied because of the considerable shock leakage and burned gas backflow through the detonation wave towards the injector nozzle. Experimental study of partially premixed RDC has been conducted by St. George et al. [6]. Their results show that higher global equivalence ratios tend to produce severe flashback events, which would lead to the prompt failure of detonation. Therefore, separate injections of the fuel and oxidizer (termed as non-

premixed RDE hereafter) can be used alternatively. However, stable detonation waves with velocity deficits up to 30% of the theoretical values were observed in the experiments of non-premixed RDE's [27]. Insufficient mixing between the separately injected propellants is one of the most important factors that cause the velocity deficits, besides the effects of multi-dimensional flows and curved detonation waves [7].

Recently, detailed measurements based on an optically accessible RDE from the USA Air Force Research Laboratory (AFRL) have been performed for a wide range of operating conditions with different experimental techniques [1,8,9]. In the rest of this paper, we term it as AFRL RDE burner for brevity. In this burner, air is injected from a plenum through a circumferential slot into an annular detonation channel and fuel is injected from a separate plenum through discrete holes evenly spaced on a circle with a circumference located near the inner edge of the annular detonation channel [1]. The height of the air slot and the diameter and number of the fuel injection holes are varied to change the air and fuel injection area, respectively.

With this facility, the non-reacting mixing of fuel and air in AFRL RDE has been studied by Rankin et al. [10]. The acetone PLIF images imply that the non-reacting flow is similar to that in an impinging jet in crossflow and a recirculation zone is observed in the outer corner of the annular channel. Furthermore, in reacting tests, Rankin et al. [1] further investigated the effects of air mass flow rate and equivalence ratio on the detonation structures using OH* chemiluminescence imaging and time-dependent static pressure measurements. Their results show

* Corresponding author.

E-mail address: huangwei.zhang@nus.edu.sg (H. Zhang).

that the speed of detonation wave varies significantly under different operating conditions. In addition, it is found that the detonation wave is present for globally stoichiometric conditions and the angle between the wave front and fuel injection surface behind the detonation is related to the fuel concentration gradients.

Hydrocarbon fuels (i.e. ethylene) were also tested in the AFRL RDE by Cho et al. [11] to understand the detonation physics and gas dynamics. Codoni et al. [12] studied the effects of back pressure on the RDE performance using simultaneous mid-IR emission and OH* chemiluminescence measurements. The ignition characteristics of the AFRL RDE were studied by Fotia et al. [13], in which four different ignition regimes were identified. In addition, the similar design to AFRL RDE is also adopted for investigating liquid-fuelled RDE at the National University of Singapore [14].

Due to the curved geometry, confined (high ratio of channel circumference to width) chamber, and fast-propagating combustion front, it is actually difficult to acquire spatially detailed and temporally simultaneous information about the flow field and detonation combustion in RDE, although the above researchers have performed very fruitful investigations. For non-premixed RDE systems, efficient mixing is one of most significant technical issues to be tackled. However, relatively limited work has been done to clarify this particular topic. With recent increased availability of high-performance computing and high-fidelity numerical schemes, numerical simulation has gradually become one of the effective methods to understand the detonation dynamics in model or simplified RDE burners [15–21]. The effects of inlet mass flow rates on H₂/air non-premixed RDE are studied by Meng et al. [17] using three-dimensional Unsteady Reynolds-Averaged Navier-Stokes (URANS) simulations. Nevertheless, it is well known that RANS cannot accurately predict the highly transient fuel/oxidizer mixing processing. Instead, Large Eddy Simulation (LES) has proven to be excellent for modelling mixing-dominated non-premixed combustion [22]. More recently, LES of the flow and mixing fields in an RDE chamber has been performed by Gaillard et al. [23], and they evaluated their injector design in terms of non-reactive H₂/O₂ mixing and total pressure recovery. Their findings from Ref. [23] were then applied as significant references for subsequent LES studies of a model RDE [24]. From the work by Gaillard et al. [23,24], one has seen the ability and potential of LES in design and fundamental research for RDE burners.

The AFRL RDE has been studied by Cocks et al. [18] using hybrid RANS-LES approach, and the predictions were in good agreement with the measured distributions of the axial mean pressure in the RDE annulus. Sato et al. [19,21] studied the AFRL RDE using LES approach, and they found that the detonation occurs under partially-premixed conditions. However, the detailed flow and mixing features, which dominate the sustainable detonation waves in RDE, were still not sufficiently explored in the above-mentioned numerical studies.

The objective of the current work is to numerically investigate the flow structure and mixing process in the AFRL RDE [1,9] using LES. A series of cases will be simulated in order to understand the various physical and geometrical influences on the non-reactive flow structure and fuel/air mixing in non-premixed RDE context, including mesh resolution, burner configuration, number of fuel injector. The rest of the paper is organized as below. In Section 2, governing equations and physical model are presented. In Section 3, the numerical results are presented and discussed. The main conclusions are summarized in Section 4.

2. Governing equation and physical model

2.1. Governing equation

The governing equations for LES can be derived through low-pass filtering their respective instantaneous equations. As such, the filtered equations of mass, momentum, species mass fraction and energy for non-reacting multi-component compressible flows can be written as

below

$$\frac{\partial \bar{\rho}}{\partial t} + \frac{\partial \bar{\rho} \tilde{u}_j}{\partial x_j} = 0, \quad (2.1)$$

$$\frac{\partial \bar{\rho} \tilde{u}_i}{\partial t} + \frac{\partial \bar{\rho} \tilde{u}_i \tilde{u}_j}{\partial x_j} = -\frac{\partial \bar{p}}{\partial x_i} + \frac{\partial}{\partial x_j} (\bar{\tau}_{ij} - \tau_{ij}^{\text{sgs}}), \quad (2.2)$$

$$\frac{\partial \bar{\rho} \tilde{Y}_m}{\partial t} + \frac{\partial \bar{\rho} \tilde{u}_j \tilde{Y}_m}{\partial x_j} = \frac{\partial}{\partial x_j} \left[\bar{\rho} D \frac{\partial \tilde{Y}_m}{\partial x_j} - \tau_{Y_m}^{\text{sgs}} \right] (m = 1, \dots, N), \quad (2.3)$$

$$\frac{\partial \bar{\rho} \tilde{E}}{\partial t} + \frac{\partial \bar{\rho}}{\partial x_j} [(\bar{\rho} \tilde{E} + \bar{p}) \tilde{u}_j] = \frac{\partial}{\partial x_j} \left[\lambda \frac{\partial \tilde{T}}{\partial x_j} + \tilde{u}_j \bar{\tau}_{ij} - H^{\text{sgs}} - \sigma^{\text{sgs}} \right], \quad (2.4)$$

where t is time and $x_j (j=1,2,3)$ is spatial coordinate component. $\bar{\rho}$ and \bar{p} are respectively the filtered density and pressure, whereas $\tilde{u}_j (j=1,2,3)$ is the filtered velocity component. N is the total number of species. The filtered viscous stress tensor $\bar{\tau}_{ij}$ is computed by using the filtered strain rate tensor \tilde{s}_{ij} . \tilde{Y}_m is the filtered mass fraction of species m and D is the molecular mass diffusivity. D is calculated through $D = \lambda / \rho C_p$ with unity Lewis number assumption. λ is the molecular thermal conductivity, and estimated using the Eucken approximation [25], i.e. $\lambda = \mu C_v (1.32 + 1.37 \cdot R / C_v)$, where C_v is the heat capacity at constant volume and derived from $C_v = C_p - R$. Here $C_p = \sum_{m=1}^M Y_m C_{p,m}$ is the heat capacity at constant pressure, and $C_{p,m}$ is estimated from JANAF polynomials [26]. R is specific gas constant and is calculated from $R = R_u \sum_{m=1}^M Y_m M W_m^{-1}$. $M W_m$ is the molar weight of m -th species and R_u is universal gas constant. μ is dynamic viscosity, and is predicted with Sutherland's law, . Here $A_s = 1.67212 \times 10^{-6} \text{kg/m} \cdot \text{s} \cdot \sqrt{\text{K}}$ is the Sutherland coefficient, while $T_s = 170.672 \text{K}$ is the Sutherland temperature. The filtered pressure \bar{p} is calculated from the perfect gas state equation

$$\bar{p} = \bar{\rho} R \tilde{T}, \quad (2.5)$$

where R is the mixture gas constant. Note that in Eq. (2.5) the sub-grid fluctuations of density and temperature are neglected. Different from the energy equation for low-Mach-number flows, the work done by the shear stress $\tilde{u}_j \bar{\tau}_{ij}$, the sub-grid enthalpy flux H^{sgs} , the sub-grid scale viscous work σ^{sgs} are included in Eq. (2.4), which are expected to be important for fully compressible flows.

The terms in Eqs. (2.1)–(2.4) with the subscripts “sgs” are unclosed and should be modelled. The sub-grid scale term τ_{ij}^{sgs} in Eq. (2.2) reads

$$\tau_{ij}^{\text{sgs}} = \bar{\rho} (u_i \tilde{u}_j - \tilde{u}_i \tilde{u}_j) = -2\bar{\rho} \mu_t \left(\tilde{s}_{ij} - \frac{1}{3} \tilde{s}_{kk} \delta_{ij} \right) + \frac{2}{3} \bar{\rho} k^{\text{sgs}} \delta_{ij} \quad (2.6)$$

where δ_{ij} is Kronecker delta function. k^{sgs} and μ_t are the sub-grid scale kinetic energy and viscosity, respectively. In the present work, they are estimated by the Wall-Adapting Local Eddy-viscosity (WALE) model [27], i.e.

$$k^{\text{sgs}} = (C_w^2 \Delta^2 / C_k)^2 (\bar{\mathcal{O}}P)^2, \quad (2.7)$$

$$\mu_t = (C_w \Delta)^2 \bar{\mathcal{O}}P, \quad (2.8)$$

in which C_k and C_w are constants and take the values of 0.094 and 0.325, respectively [27]. $\Delta = \sqrt[3]{V}$ is the nominal filter width, where V is the volume of LES cells. In Eqs. (2.7) and (2.8), $\bar{\mathcal{O}}P$ is estimated through

$$\bar{\mathcal{O}}P = \frac{(s_{ij}^d s_{ij}^d)^{3/2}}{(\tilde{s}_{ij} \tilde{s}_{ij})^{5/2} + (s_{ij}^d s_{ij}^d)^{5/4}} \quad (2.9)$$

with s_{ij}^d as below

$$s_{ij}^d = \tilde{s}_{ik} \tilde{s}_{kj} + \tilde{\Omega}_{ik} \tilde{\Omega}_{kj} - \frac{1}{3} \delta_{ij} [\tilde{s}_{mn} \tilde{s}_{mn} + \tilde{\Omega}_{mn} \tilde{\Omega}_{mn}], \quad (2.10)$$

in which $\tilde{\Omega}_{ij}$ is the anti-symmetric part of the gradient of the filtered velocity $\nabla \tilde{u}$. The WALE model is based on the square of the velocity gradient tensor which accounts for the effects of both the strain and the rotation rate of the smallest resolved turbulent fluctuations to produce the correct scaling at the wall without the explicit use of the local wall

distance [27]. It has been shown that the WALE model is able to yield better results compared to the dynamic Smagorinsky model for spatially-evolving compressible turbulent boundary layer, especially predicting the mean temperature profile at the wall [28]. In addition, the WALE model has also been successfully used in turbulent impinging jets with considerable compressibility effects [29].

The sub-grid species mass flux in Eq. (2.3) is approximated using an eddy-diffusivity model, i.e.

$$\tau_{m_i}^{\text{sgs}} = \bar{\rho} (u_i \tilde{Y}_m - \tilde{u}_i \tilde{Y}_m) = -\bar{\rho} D_t \nabla \tilde{Y}_m, \quad (2.11)$$

where D_t is the turbulent diffusivity modeled as $\bar{\rho} D_t = \mu_t / Sc_t$, and the turbulent Schmidt number is set as $Sc_t = 0.7$.

The sub-grid enthalpy flux H^{sgs} and the sub-grid viscous work σ^{sgs} in Eq. (2.4) are estimated respectively as

$$H^{\text{sgs}} = -\frac{\mu_t C_p}{Pr_t} \frac{\partial \tilde{T}}{\partial x_j} - (\mu_t + \mu) \frac{\partial k^{\text{sgs}}}{\partial x_j}, \quad (2.12)$$

$$\sigma^{\text{sgs}} = u_i \tau_{ij}^{\text{sgs}}, \quad (2.13)$$

where the turbulent Prandtl number is set as $Pr_t = 0.9$. Noted that the sub-grid total energy E^{sgs} is calculated as

$$E^{\text{sgs}} = \bar{\rho} (u_i \tilde{E} - \tilde{u}_i \tilde{E}) = H^{\text{sgs}} + \sigma^{\text{sgs}} \quad (2.14)$$

The above governing equations are solved with a multi-component reactive LES solver *RyrhoCentralFOAM* developed based on OpenFOAM 5.0 [30]. The second-order backward scheme is used for time integration and the time step is adjusted to ensure that maximum CFL number in the entire domain is < 0.2 , approximately corresponding to the time step of 10^{-9} s. The diffusion terms are calculated using second order central differencing scheme. For the convection terms, the second-order semi-discrete and non-staggered KNP [31] scheme is used. In a CFD cell V , Gauss's divergence theorem can be written as (using the instantaneous variable notation)

$$\int_V \nabla \cdot [\mathbf{u}\Psi] dV = \int_S [\mathbf{u}\Psi] dS \approx \sum_f \phi_f \Psi_f \quad (2.15)$$

Here Ψ is a generic variable, e.g. ρ , ρu_i , ρE , and p . is the velocity vector. S denotes the surface of the CFD cell. $\phi_f = \mathbf{S}_f \cdot \mathbf{u}_f$ is the volume flux across the surface f . Σ_f in Eq. (2.15) means the summation over all the surfaces of the CFD cell V .

The sum of the flux has three components [30,31]

$$\sum_f \phi_f \Psi_f = \sum_f = [\alpha \phi_{f+} \Psi_{f+} + (1 - \alpha) \phi_{f-} \Psi_{f-} + \omega_f (\Psi_{f+} - \Psi_{f-})], \quad (2.16)$$

inward flux outward flux weighted diffusion term

where α is the weighting factor. For KNP scheme, biasness is introduced in the upwind direction, depending on one-sided local speed of sound. The first and second terms of the RHS of Eq. (2.16) denote the inward and outward fluxes, respectively. The third term is a diffusion term weighted by a volumetric flux ω_f . To ensure the numerical stability, van Leer limiter [32] is needed for correct numerical flux calculations with KNP scheme.

The numerical strategy in *RyrhoCentralFOAM* has been validated with non-reacting supersonic flows, one- and two-dimensional detonation propagation [33]. It has already been successfully applied to modelling supersonic flows [34–37] and two-dimensional RDE's [38].

2.2. Physical model, computational domain and boundary condition

The rotating detonation dynamics in modular 6-inch non-premixed RDE is experimentally investigated in the AFRL [1,9]. The test rig is schematically shown in Fig. 1(a), whereas the photo of this burner when it is running is shown in Fig. 1(b). It consists of fuel plenum, air plenum and detonation channel (or interchangeably termed as RDE combustor). Non-premixed detonation is considered here and therefore

the fuel (i.e. 100% H_2) and oxidizer (i.e. air) are injected separately in the experiments. Specifically, air is injected into the RDE combustor from the upstream plenum through a circumferential slot with the diameter being 1.23 mm. The height of the air injection slot is 1.8 mm. Hydrogen is injected from a separate plenum through orifices (diameter 0.89 mm) uniformly spaced on a ring with a circumference (134 mm) near the inner edge of the annular detonation channel. The number of the fuel injectors is 120 or 80 in various experiments. The inner and outer diameters of the detonation channel are 138.7 mm and 153.9 mm, respectively. Therefore, the channel width is 7.6 mm. The height of the RDE combustor is about 102 mm. The RDE combustor is connected to the open environment through a circular channel (indicated as ‘‘Exhaust’’ in Fig. 1a).

Two different types of computational domains will be investigated, i.e. full-scale burner and a periodic burner sector with five fuel injectors. Configurations originally correspond to 80 and 120 fuel injectors in total will be considered in the foregoing burner sector and/or full burner. Note that due to the small annular RDE chamber width compared to its diameter and the limited radial variation within the flow, the curvature effect on the flow field and mixing is ignored in the case of five fuel injectors. The full-scale computational domain is shown in Fig. 2(a). The dimensions of the domain are consistent with those in the experiment [1], except for some local differences between the upper air injector confinement and the outer wall of the center-body, which are believed to have negligible influences on the present study. For the air plenum and fuel plenum, their start planes are both from -0.02 m, as can be found in Fig. 2(a).

The computational domain of a periodic burner sector with five fuel injections extracted from the full scale RDE is presented in Fig. 2(b). The distance between neighboring injectors are determined based on the practical dimensions, i.e. 80 or 120 holes in total and the width of the burner sector is proportionally determined based on the full burner. This geometry is expected to be sufficiently representative to understand the aerodynamic interactions between crosswind supersonic air streams and fuel jets, as well as the interactions between the neighboring fuel jets. Note that, due to the reduced geometry, the periodic burner in Fig. 2(a) can render us the opportunity to investigate the local flow and mixing fields with fine mesh distributions. This strategy is also used by Sato et al. for their simulations of the same burner [19], in which the general flow structures observed in the experiments are well captured. The comparisons between two computational domains used in the present work will be mentioned in Section 2.4 and discussed in Section 3.

Proper mesh generation strategy should be used due to the complex geometry as shown in Fig. 2 and also the necessity to maintain relatively high fidelity and avoid the numerical errors caused by the poor mesh quality. In our work, the method termed as *SnappyHexMesh* from OpenFOAM package is used [39]. The *snappyHexMesh* utility generates three-dimensional meshes containing hexahedra and split hexahedra from a triangulated surface geometry for complex geometries. For the AFRL RDE burner, hexahedra cells are used to discretize the domains in Fig. 2, which are schematically shown in Fig. 3. A background computational mesh size of 0.5 mm is used. Local mesh refinement with different refinement levels is performed in the surface-normal direction and mixing region with high gradients of velocity and/or temperature. These areas may have intensive mixing between injected fuel and air and also complicated flow topological structures based on the experimental observations [1,9,40]. The mesh size near the wall and mixing region is the order of 10^{-5} m, and the y^+ values range from 0.68 to 2.1. Besides, a baseline computational grid with cell size of 2×10^{-4} m has been used in the LES study of Sato et al. [19] with the same configuration. In our simulations, the mesh size near the wall is much finer than that used in Ref. [19]. The specific information about the mesh information will be tabulated in Section 2.4 and discussed in Section 3.

The inlet boundary conditions in the present simulations are consistent with the selected cases from the experiments [1]. For both

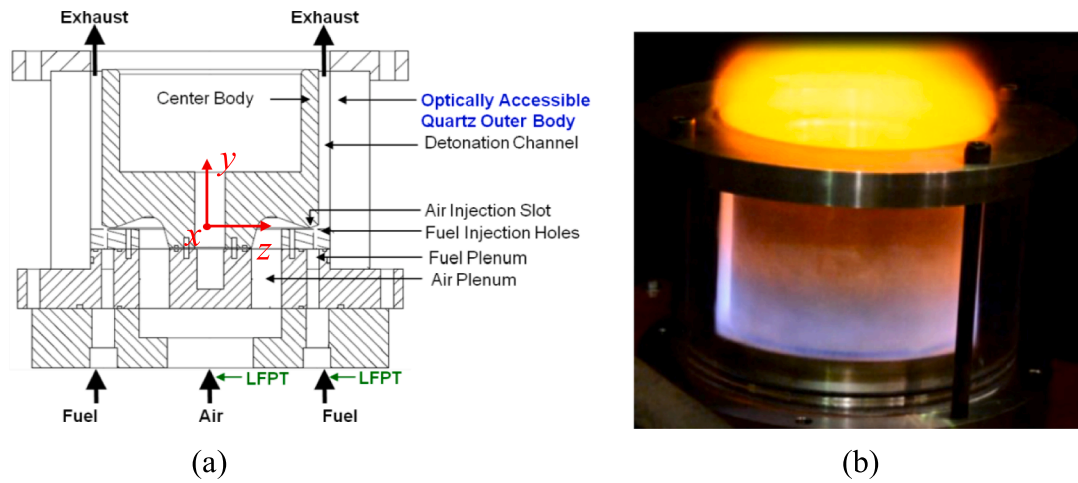


Fig. 1. (a) Schematic of the AFRL RDE and (b) visible photograph during operation [1].

geometries in Fig. 2 (i.e. full burner and periodic burner sector), the boundaries include fuel inlet, air inlet, channel and plenum walls and outflow (marked in Fig. 2). For both air and fuel inlets, the conditions are specified through matching the experimental measurements, i.e. the specific mass flow rate, temperature and pressure from the experiments [9]. It should be noted that relatively low Mach number (< 0.3) is obtained based on the mass flow rates of fuel and air. In addition, the turbulent flow statistics are not measured, and the inlet is relatively far upstream relative to the combustor. Therefore, no turbulence is included in our boundary inlets. The outflow is set as non-reflective boundary, while the RDE channel and plenums are non-slip walls. For

burner sector case, the lateral boundaries are assumed to be periodic, as seen in Fig. 2(b).

2.3. Simulation case

In the current work, we will investigate the influences of the mesh resolution, fuel injector spacing, mass flow rate and also computational domain on fuel/air mixing in the AFRL RDE burner, and therefore a series of comparative simulations are conducted. Their detailed information is tabulated in Table 1. For all the cases, the total temperatures of the fuel and air streams are 300 K and the global equivalence

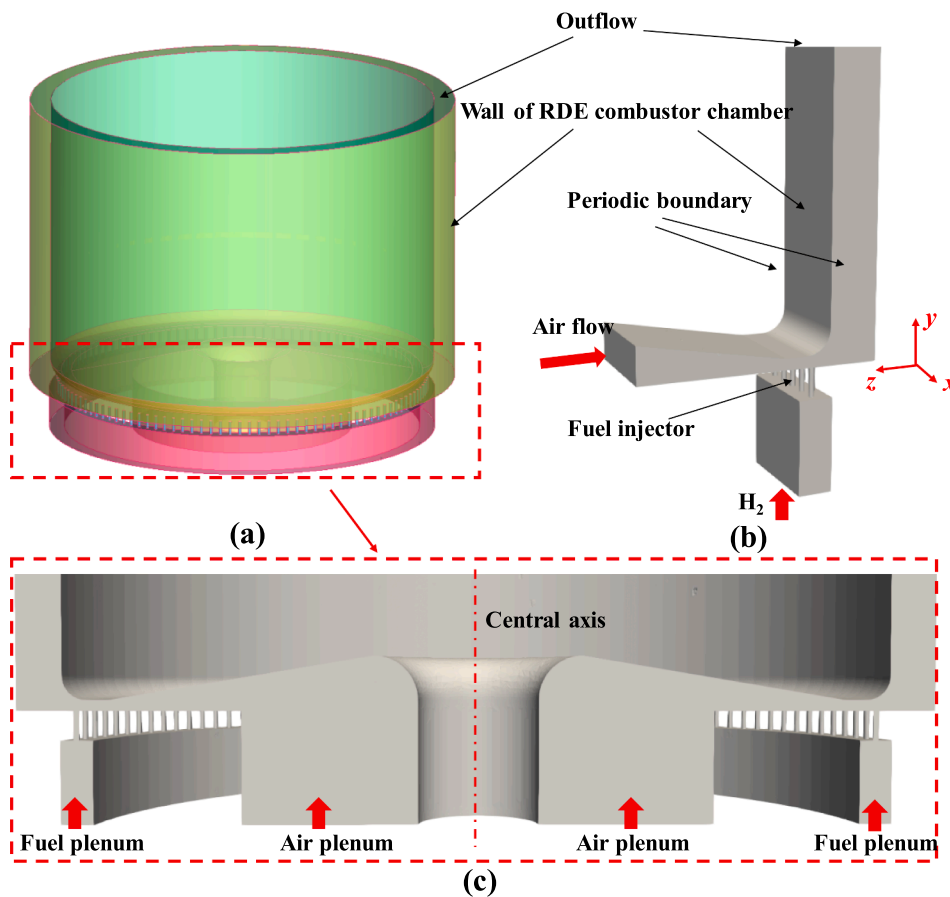


Fig. 2. Schematic of the computational domain: (a) full scale AFRL RDE, (b) periodic RDE burner sector with five fuel injection orifices and (c) an enlarged view of the central plane including fuel and air plenums.

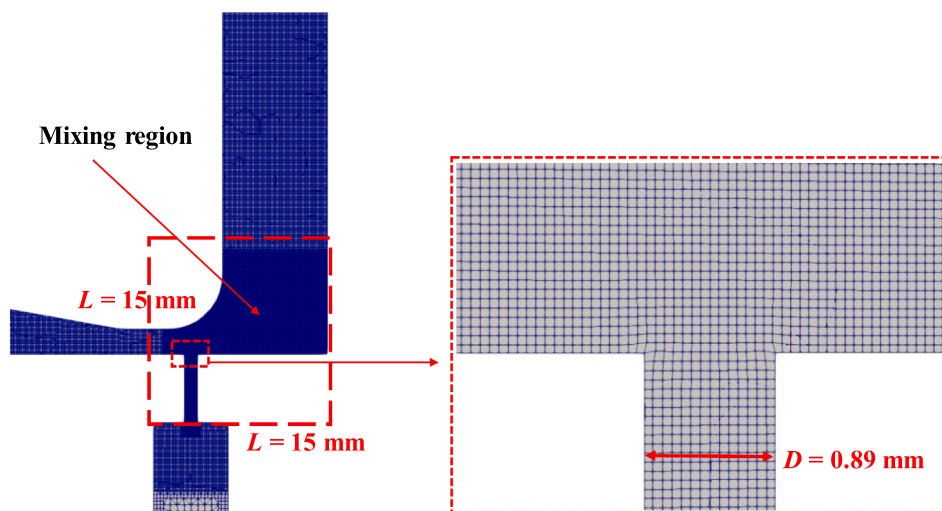


Fig. 3. Schematic of mesh distributions on the central plane of fuel jet and mesh resolution close to fuel inlet.

Table 1
Information for the simulated cases.

Cases	Mesh size in the mixing region (mm)	Total number of cells (million)	Simulated/ total number of injection orifices	Air flow rate (kg/s)	Fuel flow rate (g/s)
Periodic burner sector	1 0.1	1.0	5/120	0.02625	0.75
	2 0.0625–0.1	2.99	5/120	0.02625	0.75
	3 0.04	9.6	5/120	0.02625	0.75
	4 0.0625–0.1	2.99	5/120	0.00625	0.18333
	5 0.0625–0.1	2.99	5/120	0.01333	0.3875
	6 0.0625–0.1	4.43	5/80	0.02	0.58125
Full scale AFRL RDE burner	7 0.0625–0.125	9.8	120/120	0.15	4.4
	8 0.0625–0.125	9.8	120/120	0.32	9.3
	9 0.0625–0.125	9.8	120/120	0.63	18

ratios are close to unity [1].

Specifically, Cases 1, 2 and 3 are used to examine the grid sensitivity for periodic burner sector. With the same background mesh, the cells in the mixing region are respectively refined to different sizes, i.e. 0.1 mm (minimum nominal cell size) in Case 1, 0.0625–0.1 mm in Case and 0.04 mm in Case 3. The resultant total cell numbers in the above three cases are 9.6 million, 2.99 million and 1.0 million, respectively. The corresponding results will be discussed in Section 3.1.

Cases 2, 4 and 5 are selected to analyze the effects of the air flow rates on the non-reacting flow and mixing characteristics, i.e. 0.15 (Case 4), 0.32 (Case 5) and 0.63 kg/s (Case 2), which correspond to the experimental test cases in Ref. [1]. Note that the mass flow rates in Case 1–6 with five fuel injectors are scaled appropriately by 5/120 or 5/80.

Also, the effects of fuel injection orifice spacing are studied with the periodic burner sector (see Fig. 2b) and analyzed with Cases 5 and 6. The distances between two neighboring fuel injectors correspond to those in the full AFRL burner with 80 and 120 fuel injectors. Specifically, their original radial distances are 5.26 mm and 3.51 mm, respectively. This leads to various widths of the five-orifice burner sector, and therefore various total cell number (shown in Table 1), although they have the same mesh resolution (i.e. 0.0625–0.1 mm).

Finally, the full-scale AFRL RDE combustor is also simulated with three air flow rates, i.e. Cases 7–9, which will be presented in Section 3.4. Note that in these three cases, the minimum nominal cell size is close to that in Case 2, i.e. 0.0625–0.1 mm, resulting in approximately 9.8 million cells. Through these three cases, we will compare the flow and mixing fields with various mass flow rates.

3. Results and discussion

3.1. Mesh sensitivity analysis

Three grids from Cases 1, 2 and 3 are used to evaluate the sensitivity of the mesh resolutions in the present simulations. Fig. 4 compares the distributions of temperature and velocity components along the x -direction near the fuel jet ($y = 10^{-5}$ m, $z = 0$ m). Note that y -direction (i.e. burner height direction) is streamwise for fuel, whilst z -direction for air stream. In general, the three meshes predict the similar profiles of temperature and velocity components. For instance, immediately downstream of each circular fuel jet, the temperature has two pronounced peaks (approximately 310 K) along the periphery of the fuel jets. Furthermore, for each fuel jet, the y -component velocity has an approximate top-hat profile and maximum value is around 900 m/s, which is very close to the local sound speed. However, for z -component velocity, two peaks can also be seen for each jet with the maximum values as high as 450 m/s.

Nevertheless, there are still some distinctions based on the results from three cases. For temperature and y -component velocity, Case 1 with coarse cells yields respectively about 2% and 10% lower values for the inter-jet regions, compared to the results from Cases 2 and 3 as shown in Fig. 4(a). For z -component velocity, Case 1 has the peak velocity lower by 100 m/s or so. The temperature and velocity components predicted in Case 2 are close to those in Case 3 (with relative error smaller than 1%). Especially for the mesh size near the wall of Case 2 and 3, it is seen that the distributions of temperature and velocity in the z -direction are independent of the mesh scale, indicating that the boundary layer at the mixing region is resolved in the present simulations. Based on the results in Fig. 4 and the foregoing discussion, we will adopt the same resolution for the mixing region as in Case 2 (cf. Table 1) for the following discussions.

3.2. Flow structure and mixing characteristics

The instantaneous vortex structures in the non-reactive AFRL RDE burner is identified through Q -criterion, which is the second invariant of the velocity gradient tensor [41]. Fig. 5 visualizes the instantaneous vortex structures with $Q = 1 \times 10^{11} \text{ s}^{-2}$ colored by the resolved hydrogen mass fraction at three instants. The flow fields around one fuel injector in the current RDE combustor are similar to those of jet in supersonic crossflow. Large scale structures including Counter-rotating Vortex Pairs (CVP), jet shear layers and horseshoe vortex are formed as the fuel jets interact with the air crossflow [42]. Interactions between those typical structures and shock waves can lead to complex vortex

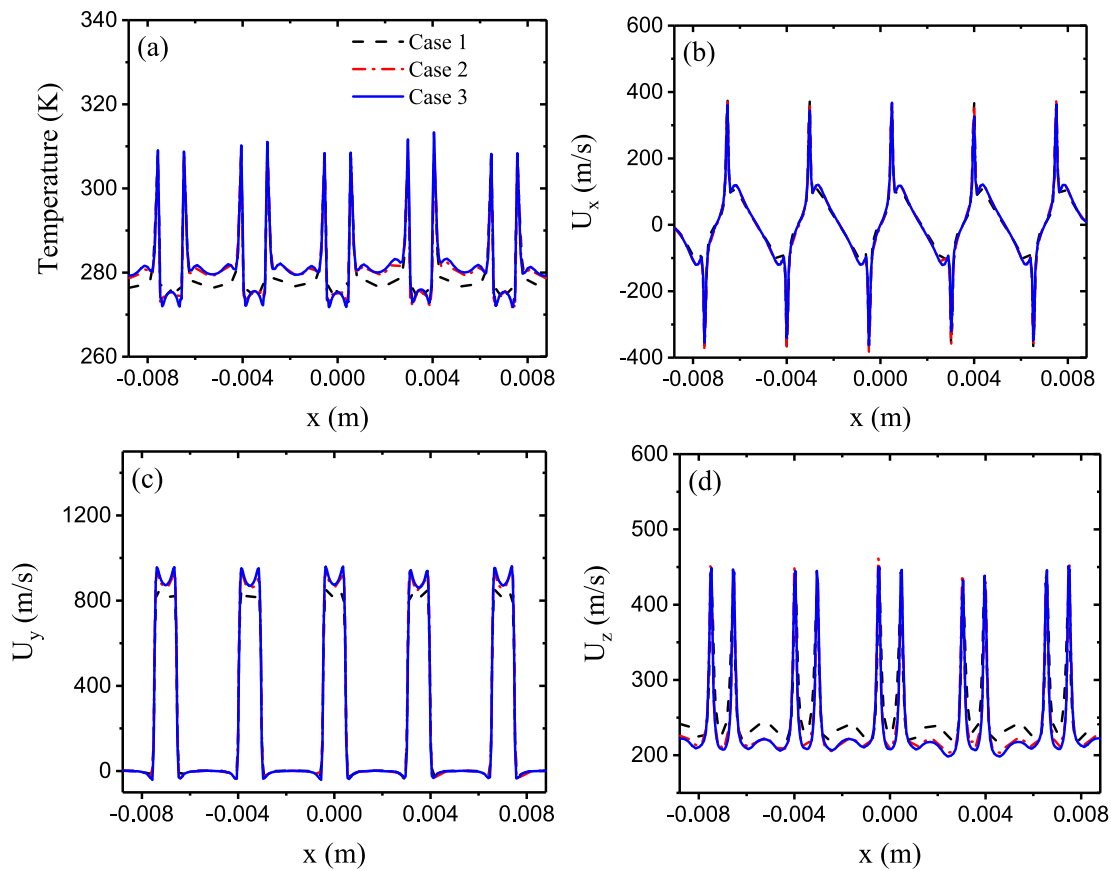


Fig. 4. Distributions of (a) temperature and (b-d) velocity along the x-direction near the fuel jet ($y = 10^{-5}$ m, $z = 0$ m) predicted with three different grids corresponding to Cases 1, 2 and 3 in Table 1.

structures, as shown in Fig. 5. After interacting with the shock wave, the large scales (marked as V1 and V2 in Fig. 5) are combined into one vortex structure (V12) and then broken into smaller structures. Similar unsteady evolution process for V3 and V4 also appears, which is not presented in Fig. 5. As such, more intense turbulence with smaller scales and more efficient mixing is expected to be observed in the mixing region near the top end of RDE combustor.

To analyze the effects of the vortex structures and shock waves on mixing at the burner top end, Fig. 6 shows the distributions of local Mach number, instantaneous hydrogen mass fraction, and density gradient magnitude ($\|\nabla\bar{\rho}\|$) on the jet central plane at the same instants as in Fig. 5. It can be seen that the velocity of the crossflow is very close

to the speed of sound, which can be confirmed by the unity local Mach number. The supersonic region ($Ma > 1$) is mainly distributed on the windward side of the fuel jet. In addition, as shown in Fig. 6, a shock wave is formed in the supersonic region and interacts with the fuel jet shear layer. The bow shock, shock wave, jet shear layer and slip line are identified by the density gradient magnitude as shown in Fig. 6(b), in which shock waves with different sizes and intensities at different instants are observed on the windward side of the hydrogen jet. The jet penetration is influenced by the shock wave, the formation of which may be related to the inflow rate of air. The interactions between the fuel jet and shock wave can enhance the turbulence intensity and thus is expected to promote the mixing process [43]. The fuel jet exhibits

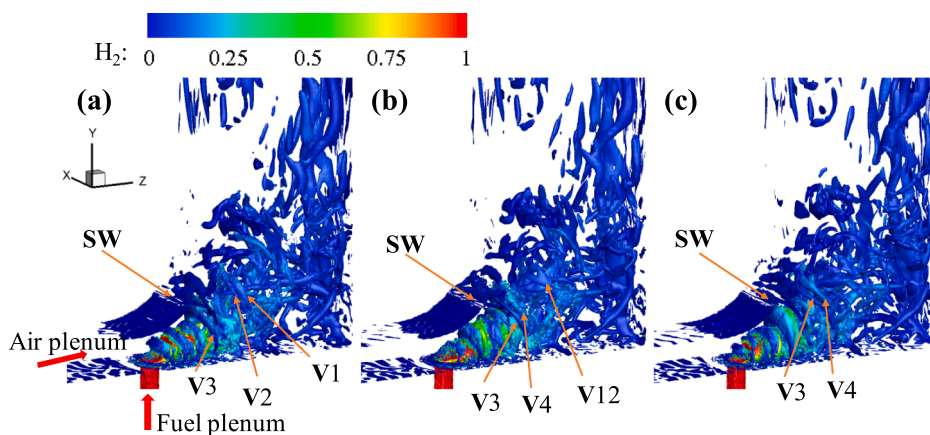


Fig. 5. Vortex structures (visualized with iso-surfaces of $Q = 1 \times 10^{11} \text{ s}^{-2}$) colored by resolved hydrogen mass fraction at different time instants: (a) t_0 , (b) $t_0 + 2 \mu\text{s}$, and (c) $t_0 + 4 \mu\text{s}$. The abbreviation SW represents shock wave, while V1, V2, V12, V3 and V4 represent vortex structures.

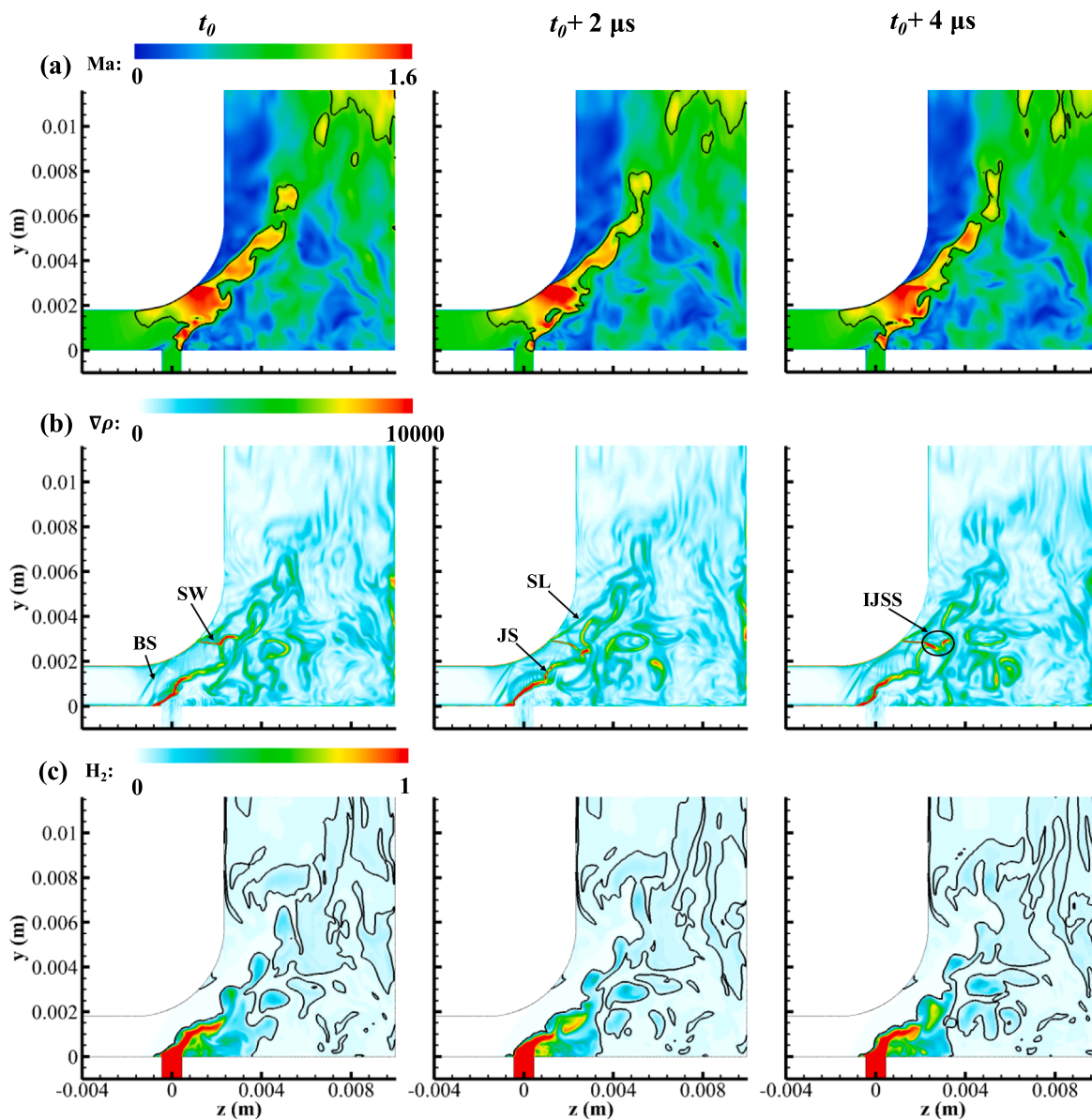


Fig. 6. Distributions of (a) local Mach number, (b) density gradient magnitude (in kg/m^4) and (c) resolved hydrogen mass fraction on the jet central plane. Three columns correspond to three time instants, i.e. t_0 , $t_0 + 2 \mu\text{s}$, $t_0 + 4 \mu\text{s}$. The abbreviations, SW, BS, JS, SL and IJSS, represent shock wave, bow shock, jet shear layer, slip line and interactions between jet shear layer and shock wave, respectively. The black lines of (a) and (c) represent the sonic and stoichiometric H_2 -air mixture, respectively.

different instantaneous mixing characteristics and more stoichiometric mixture can be found in the mixing region near the top end of RDE combustor with intense turbulence and large number of small-scale structures. Moreover, the stoichiometric mixture is mainly distributed in the subsonic region.

Fig. 7 shows the distributions of time averaged pressure with streamlines, time averaged hydrogen mass fraction, root-mean-square (RMS) values of hydrogen mass fraction (calculated based on the resolved field) and turbulent kinetic energy on the jet central plane ($x = 0$). Note that the turbulent kinetic energy presented in Fig. 7(d) includes both resolved and sub-grid turbulent kinetic energies. Four recirculation zones, i.e. R1, R2, R3 and R4, are observed in Fig. 7(a). The recirculation zone R1 is related to the horseshoe vortex upstream of fuel jet. The recirculation zone R2 is located in the leeward side of the fuel jet and is related to the entrainment of the large-scale CVPs. The recirculation zone R3 lies near the top end of RDE combustor and is caused by the confinement of the RDE channel. The recirculation zone R4 is located between the slip line and inner wall of the combustor.

Note that R3 and R4 are relatively large and expected to play significant role in local fuel/air mixing. Similar mean flow structures were also observed using RANS of a model non-premixed RDE burner by Zheng et al. [44].

In Fig. 7(b), one can find that high hydrogen mass fraction only exists near the jet exit, and it decays very quickly. This implies that the efficient mixing occurs in the RDE top end due to the high-speed crosswind streams and complicated flow structures as analyzed in Fig. 6. The stoichiometric isolines lie at the top end of the RDE burner, as indicated in Fig. 7(b). It should be acknowledged that the field is not sufficiently converged close to the two recirculation zones, i.e. R3 and R4, due to the strong flow unsteadiness there. The occurrence of efficient mixing can also be confirmed by the distribution of root-mean-square (RMS) values of hydrogen mass fraction in Fig. 7(c): finite values are only observable near the jet exit. Furthermore, considerable turbulence occurs in the near field of fuel jet, indicating that the mixing process in the near field is dominated by large-scale structures, which can be seen in Fig. 5. It should be noted that the RMS values of

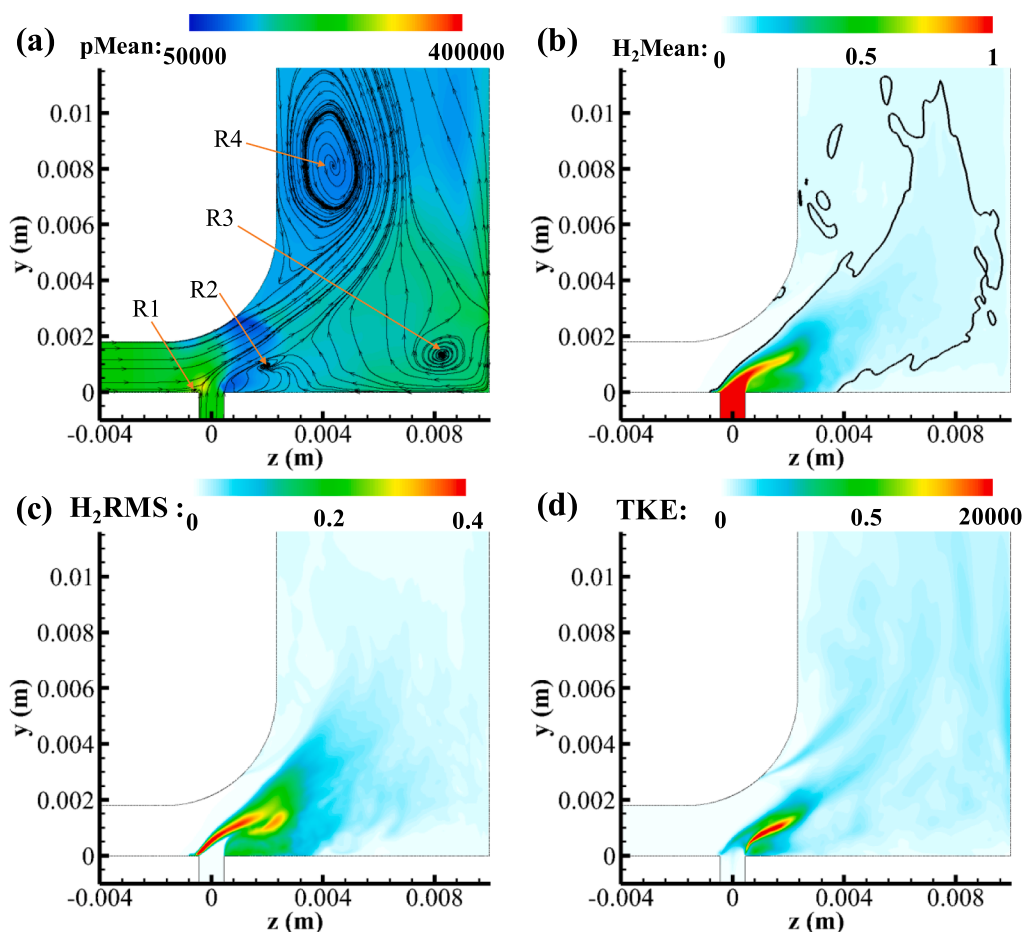


Fig. 7. Distributions of (a) time averaged pressure (in Pa) with streamline, (b) time averaged hydrogen mass fraction, (c) root-mean-square value of hydrogen mass fraction and (d) turbulent kinetic energy (in m^2/s^2). The regions marked as R1, R2, R3 and R4 in (a) are recirculation zones. The black lines in (b) represent the stoichiometric H_2 -air mixture.

hydrogen mass fraction and turbulent kinetic energy in the region after the interaction point (marked with IJSS, see Fig. 6b) between the shock wave and jet shear layer are rapidly decreased, and the region mostly has the stoichiometric mixture.

Based on the OH^* chemiluminescence images made by Rankin et al. [1], the heights of the rotating detonation fronts can be as high as 0.08 m. Therefore, one can expect that an individual detonation front may be chemically active simultaneously in fuel-rich, stoichiometry and fuel-lean composition from the top end to the exhaust direction in the non-premixed RDE. In the discussed case, the height for stoichiometric fuel/air composition is about 0.01 m, as shown in Fig. 7(b). Therefore, about 87% of the detonation front height may run under fuel-lean condition, based on the current non-reacting results. This can be qualitatively confirmed by the various levels of OH^* signal intensities: generally, the lower in the channel, the stronger the OH^* chemiluminescence and therefore chemical reactions [1]. It should be acknowledged that some differences may exist in terms of the reactant mixing between non-reacting and reacting flows. These may be related to the thermal expansion, transport property variation and/or localized turbulence modulation due to the combustion heat release. Therefore, the results of the non-reacting flows only offer a qualitative reference for reacting RDE analysis. For full understanding the mixing characteristics in detonative combustion field, LES of reacting RDE's should be performed.

In Fig. 5-7, flow structures and mixing behaviors of only one fuel jet are analyzed. In practical RDE burners, propellant injectors are always closely placed, e.g. in AFRL RDE burner. To discuss the instantaneous interactions between the fuel jets, Fig. 8 shows the resolved hydrogen mass fraction and temperature on the central plane of five fuel jets in periodic burner sector. It should be highlighted that since the distributions of the fuel jets are uniform in the circumferential direction

for AFRL RDE burner, the statistical results on the central plane of each jet nearly have the same features. They have been named as Injectors -1, -2, 0, 1 and 2, respectively. Injector 0 is the middle one discussed in Fig. 5-7. The tilting direction of each jet is different, probably due to the different interactions between the high-speed air flows and the jets. This may directly affect passage of the high-speed oxidizer in the channel between the fuel jet and rounded inner walls, which would further influence the mixing in the RDE channel. Shock waves with different sizes are observed on the windward side of the jet plume. The jet penetration is influenced by the shock wave, the formation of which may be related to the inflow rate of air. It can also be seen that each fuel jet shows different instantaneous mixing characteristics, visualized with the iso-lines of stoichiometric composition. Although the mean height of stoichiometric fuel/air composition is about 0.01 m, however, beyond that there are still lots of stoichiometric pockets transported from the fuel jets. These may lead to the instability or different reactivity levels of the propagating detonation front, as demonstrated by some OH^* chemiluminescence images [1].

Besides the compositional non-uniformity in height direction discussed in Fig. 7, the non-uniformity in azimuthal direction between two neighboring jets (spacing 3.51 mm) can also be observed from Fig. 8. Therefore, when the RDE is running, the detonation front may periodically sweep in different composition, which is particularly true for the base of the detonation front at the RDE top end. From the simplified numerical simulations performed by Fujii et al., it was found that significant velocity reduction, up to 86% of the CJ (Chapman-Jouguet) velocity, can occur [45], and this would considerably affect the RDE propulsive performance. Compositional non-uniformity has already been shown to be an important topic for fundamental research on detonation, e.g. in Refs. [46,47], and in the RDE context it will be discussed further in our following LES when reacting RDE is considered.

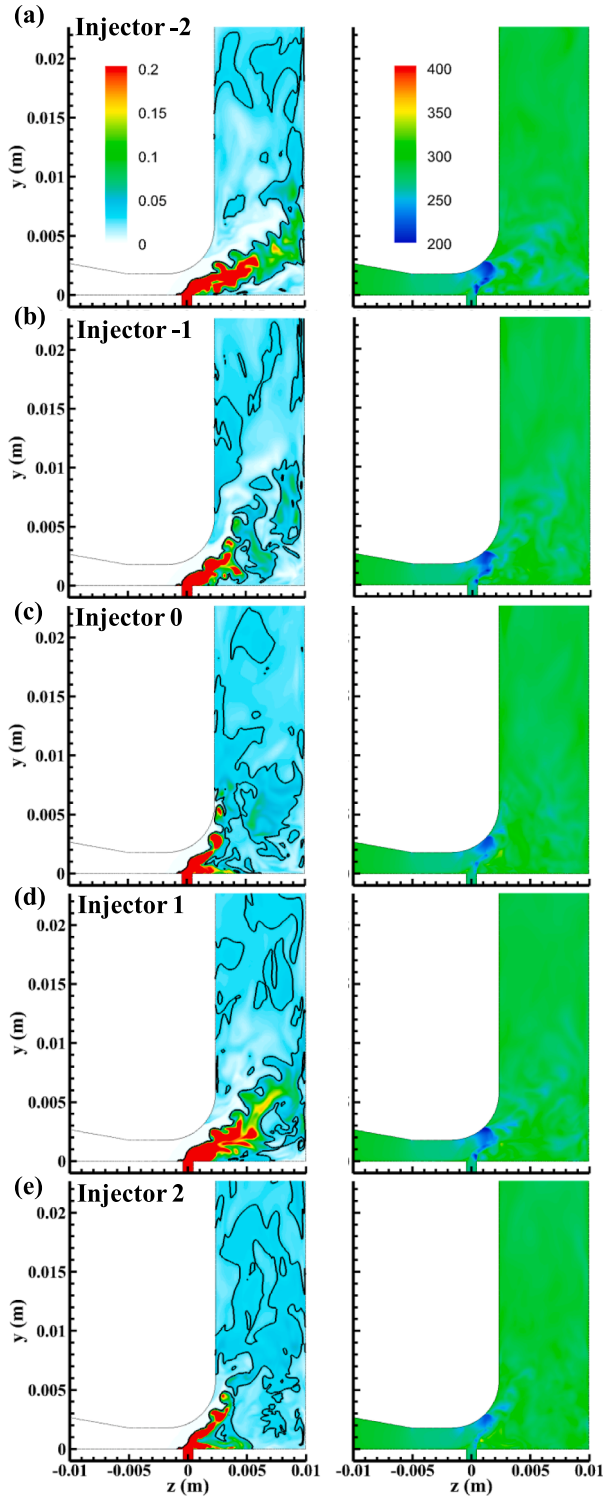


Fig. 8. Distributions of resolved hydrogen mass fraction (left column) and temperature (in K, right column) on the central plane of five jets (from a-e). The black lines in the first column are the stoichiometric H₂/air composition.

3.3. Fuel and air mass flow rate

In this Sub-section, the effects of fuel and air mass flow rates on the overall mixing characteristics will be quantitatively discussed. Firstly, the mixing efficiency η_{mix} is introduced to quantify the fuel/air mixing process in this AFRL RDE burner. It is defined as the ratio of the effective mass flow rate of burnable hydrogen \dot{m}_{mixing} to total hydrogen

mass flow rate \dot{m}_{total} at a given cross section along the burner height direction (y direction) [48]

$$\eta_{mix} = \frac{\dot{m}_{mixing}}{\dot{m}_{total}} = \frac{\int_S \langle \tilde{Y}_{react} \rangle \langle \tilde{\rho} \rangle \langle \tilde{u}_n \rangle dA}{\int_S \langle \tilde{Y}_{H_2} \rangle \langle \tilde{\rho} \rangle \langle \tilde{u}_n \rangle dA}, \quad (3.1)$$

where $\langle \tilde{Y}_{react} \rangle$ is the time averaged burnable H₂ mass fraction can be calculated as

$$\langle \tilde{Y}_{react} \rangle = \begin{cases} \langle Y_{H_2} \rangle & \langle Y_{H_2} \rangle \leq Y_{stoic} \\ Y_{stoic} \frac{1 - \langle Y_{H_2} \rangle}{1 - Y_{stoic}} & \langle Y_{H_2} \rangle > Y_{stoic} \end{cases} \quad (3.2)$$

$\langle Y_{H_2} \rangle$ is the time averaged mass fraction of hydrogen. In Eq. (3.1), $\langle \tilde{\rho} \rangle \langle \tilde{u}_n \rangle dA$ represents the fluid mass flow rate at a given cross section along y-direction and S is the area of the considered cross section in the RDE combustor. Y_{stoic} is fuel mass fraction under stoichiometric condition, which is approximately 0.0283 in the present study. From Eq. (3.2), one can see that for fuel-lean locations, all the H₂ is assumed to be burnable, whereas for fuel-rich locations, the burnable H₂ is estimated based on the available oxidizer. When η_{mix} equals unity, it means the fuel and air are perfectly mixed, while if it equals zero, this implies that they are not mixed.

The mixing efficiency η_{mix} of Cases 2, 4 and 5 is calculated based on Eqs. (3.1) and (3.2), to examine the effects of the various fuel and air mass flow rates. It should be mentioned that from Case 4, Case 5 to Case 2, fuel and air flow rates gradually increase with fixed global equivalence ratio being about unity (as tabulated in Table 1). Fig. 9 shows the variations of mixing efficiency along the y-direction in three cases. The reader should be reminded that y = 0 in Fig. 9 corresponds to the bottom wall of the RDE channel. It can be seen that the mixing process mainly occurs near the top end of the RDE combustor. The heights of the mixing region h can be estimated based on the location off the bottom where the mixing efficiency first reaches unity. The heights in the three cases have been indicated in Fig. 9. They are 0.01 m, 0.019 m and 0.024 m, respectively, accounting for 9.8%, 18.6% and 23.5% of the whole burner height. In general, shorter height means quicker mixing and better spatial uniformity in the downstream region of the RDE chamber. It should be noted that when rotating detonation is initiated, the downstream of the RDE channel would not have lots of residual H₂ due to propagating detonation wave and therefore here only the mixing characteristics near the top end of burner, i.e. 0 < y < 0.025 m, are relevant and indicative for reactive case.

In addition, in all the three shown cases, mixing efficiency demonstrates non-monotonic spatial variation from the bottom (y = 0) to the

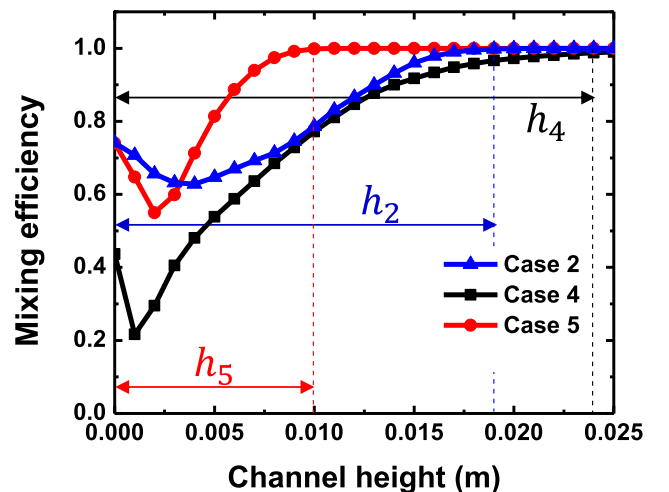


Fig. 9. Mixing efficiency along the y-direction in Cases 2, 4 and 5. The quantity h_i indicates the height of the mixing region in the RDE channel.

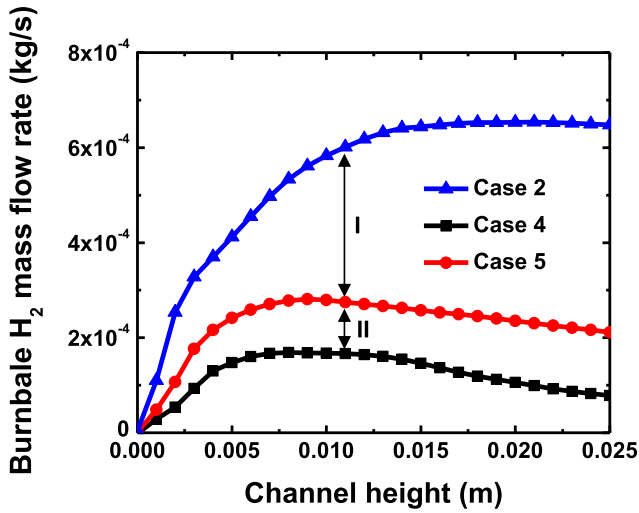


Fig. 10. Burnable hydrogen mass flow rate along the y -direction in Cases 2, 4 and 5.

channel. Specifically, along the height direction, η_{mix} first decreases and then quickly increases, approaching the stoichiometric global equivalence ratio. The first decrease was not observed from the LES of their RDE burner by Gaillard [23] and this enhanced mixing may be due to the recirculation zone R2 as indicated in Fig. 3. When y is very small, higher mass flow rates, e.g. in Case 2, lead to higher overall mixing efficiency. Nevertheless, when y is relatively large, η_{mix} shows higher values for Case 5, which has the intermediate mass flow rates. Also, their values of η_{mix} are close in Cases 2 and 4. Overall, Case 5 has the best mixing efficiency, while Case 4 has the lowest. Therefore, mixing efficiency does not correlate positively with mass flow rates and an optimal mass flow rate may exist for individual equivalence ratios.

The effective mass flow rate of burnable hydrogen \dot{m}_{mixing} in different cross sections along y -direction is also presented. As shown in Fig. 10, although Case 2 with the highest air flow rate does not have the best mixing efficiency, however, it has the most burnable hydrogen (highest \dot{m}_{mixing}) is observed for the whole height. This may result from its high mass flow rate of hydrogen. As shown in Table 1, the fuel flow rates from Cases 4, 5 and 2 are consecutively doubled, the burnable hydrogen increases by 68% for Case 5 (indicated by II in Fig. 10) and 118% for Case 2 (indicated by I in Fig. 10), respectively, if we take $y = 0.011$ m as an example. Therefore, \dot{m}_{mixing} increases with the fuel mass flow rate.

The fluctuations of reactant mass fraction in an RDE have important effects on the initiation and stable propagation of detonation wave [23]. The RMS of the hydrogen mass fraction spatially averaged in a given cross section along the height direction can be estimated from

$$\{\sqrt{Y_{H_2}^2}\} = \frac{\int \sqrt{Y_{H_2}^2} \langle \bar{\rho} \rangle \langle \bar{u}_n \rangle dA}{\int \langle \bar{\rho} \rangle \langle \bar{u}_n \rangle dA}. \quad (3.3)$$

Based on Eq. (3.3), the variations of surface averaged RMS of H_2 mass fraction $\{\sqrt{Y_{H_2}^2}\}$ are shown in Fig. 11. One can see that Case 5 has the minimal fluctuations of H_2 mass fraction, which means that a more stable propagation of detonation wave may exist under that condition. This is in line with the results in Fig. 9, which shows that mixing efficiency of Case 5 is the highest. Experimental results of Rankin et al. [1] suggest that the standard deviation of the detonation wave speed of Case 5 is the smallest compared with Cases 2 and 4, which is loosely consistent with the findings from our non-reacting LES results. For the surface averaged turbulent kinetic energy (calculated with the similar method to Eq. (3.3)), Case 2 with biggest mass flow rate has the highest energy than the other two, whilst Cases 4 and 5 are close to each other.

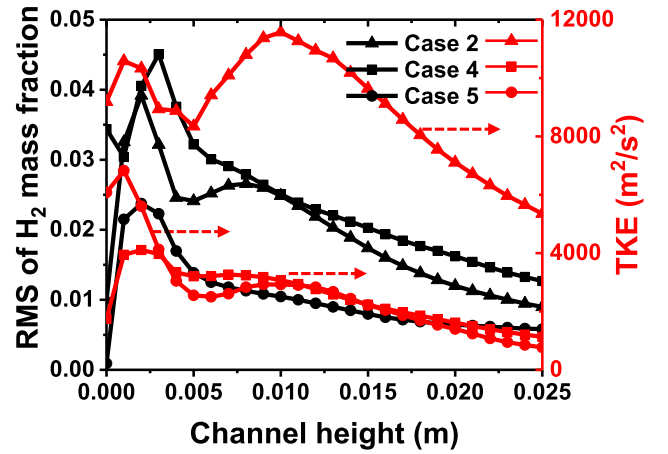


Fig. 11. Surface averaged RMS of hydrogen mass fraction and TKE in Cases 2, 4 and 5.

The distributions of surface averaged equivalence ratio along the y -direction (RDE chamber height direction) in Cases 2, 4 and 5 are shown in Fig. 12. They are estimated through averaging the resolved values on different cross sections along the burner height direction (y -direction). The surface averaged equivalence ratio increases rapidly (leading to localized fuel-rich area) along the y -direction and then slowly decreases to the global equivalence ratios. Note that the global equivalence ratios of our simulated cases are close to stoichiometry. Insufficient mixing at the top end region ($y < 0.008$ m) is observed with local fuel-rich conditions. By comparing Cases 2, 4 and 5 with different mass flow rates, it can be found that the Case 5 with intermediate mass flow rate has the lowest equivalence ratio at the top end region.

Propagating detonation wave would not be self-sustaining in too lean or rich fuel mixtures; instead, it only occurs within a range of equivalence ratios. Two stand-alone simulations based on *Shock & Detonation Toolbox* [49] and *RYrhoCentralFOAM* are performed here. The detonation temperature and propagation speed as functions of equivalence ratio are shown in Fig. 13. For the following analysis, we assume that the H_2 /air mixture with equivalence ratio being 0.6–2.0. This range (marked by the detonability range in Fig. 13) corresponds to high temperature and propagating speed of the detonation front.

As such, in the current LES of RDE burners, the nominal detonability area ratio ϕ is introduced to indicate the possible area where the self-sustaining detonation wave can exist in the AFRL RDE burner. It is

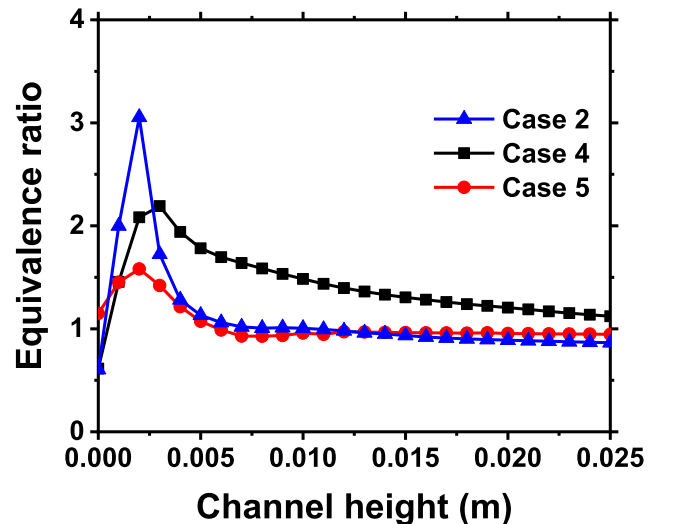


Fig. 12. Surface averaged equivalence ratio along the y -direction in Cases 2, 4 and 5.

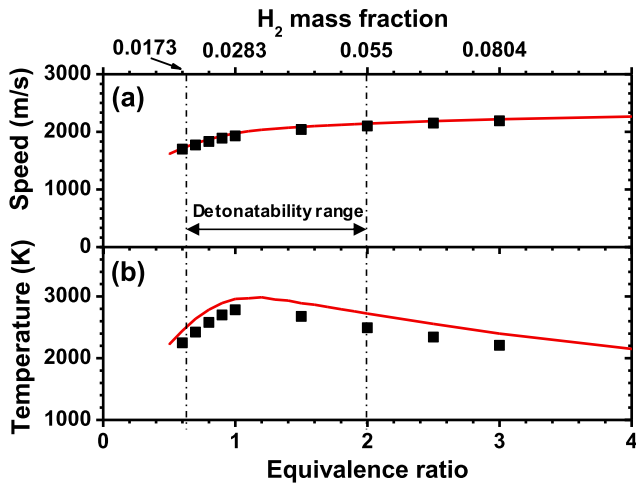


Fig. 13. (a) Propagating speed and (b) temperature of detonation wave in hydrogen/air mixture as functions of equivalence ratios. Lines: results from Shock & Detonation Toolbox [49]; Symbols: results from one-dimensional detonation tube calculations with *RYrhoCentralFOAM*. The mechanism for H_2 /air mixture by Choi et al. [50] is used for both calculations.

defined as

$$\phi = \frac{\int \gamma dA}{\int dA}, \quad \gamma = \begin{cases} 1, & \text{if } 0.02 < \langle \tilde{Y}_{H_2} \rangle < 0.055 \\ 0, & \text{otherwise} \end{cases} \quad (3.4)$$

Fig. 14 shows the evolution of detonability area ratios ϕ along the y -direction. One can see that, for $y < 0.015$ m, Case 5 has the highest detonability area ratio, whilst Case 4 corresponds to the lowest. This tendency is consistent with what is seen from Fig. 9. Beyond this range, i.e. $y \geq 0.015$ m, the ratios in the three cases are close to each other and approach unity, indicating that there the hydrogen mass fraction fall in the range of the detonability limits.

Fig. 15 shows the comparisons of mixing efficiency (i.e. η_{mix} calculated with Eq. (3.1)) from Case 5 and Case 6. In generally, Case 6 has better mixing efficiency than Case 5. The height of mixing region for Case 6 is 0.0075 m, while that for Case 5 is 0.01 m. Within the mixing region, η_{mix} in Case 6 is consistently higher than that in Case 5. In addition to the mixing efficiency, the effective mass flow rate of burnable hydrogen \dot{m}_{mixing} in different cross sections along the height direction is also presented in Fig. 16. It is clear that the burnable hydrogen \dot{m}_{mixing} of Case 6 with a total number of 80 injection orifices is larger than Case 5 with a total number of 120 injection orifices, even if they have the

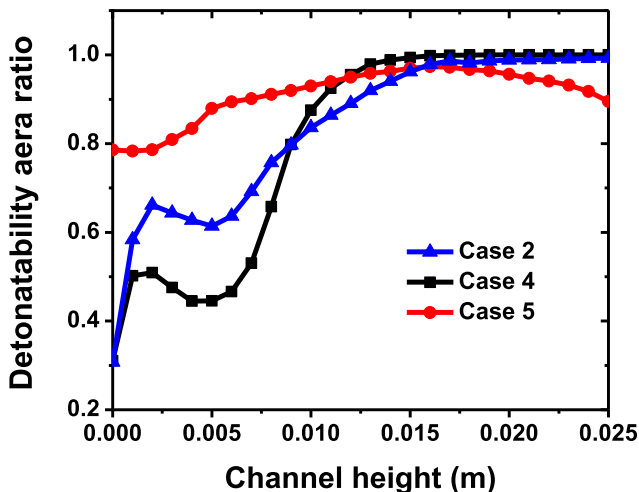


Fig. 14. Detonability area ratio along the y -direction in Cases 2, 4 and 5.

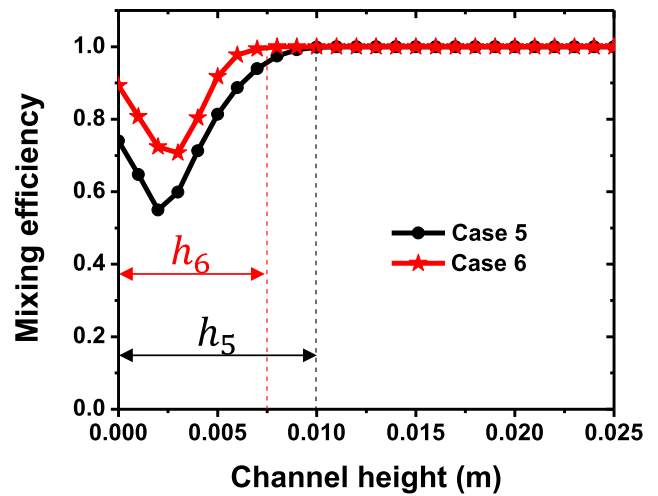


Fig. 15. Mixing efficiency along the y -direction in Cases 5 and 6. The quantity h_i indicates the height of the mixing region in the RDE channel.

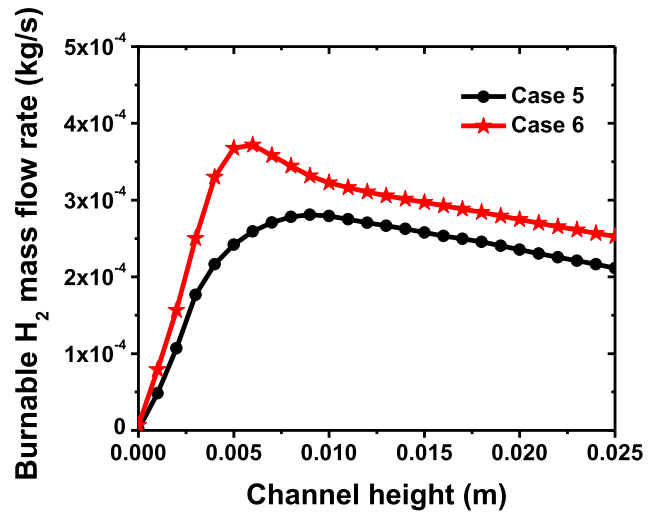


Fig. 16. Burnable hydrogen mass flow rate along the y -direction in Cases 5 and 6.

same air flow rate. Moreover, the surface averaged equivalence ratios in Cases 5 and 6 are compared in Fig. 17. It is shown that the surface averaged equivalence ratio in Case 5 is slightly higher than that in Case 6 for $y < 0.007$ m, indicating that Case 6 generally has better mixing efficiency than Case 5 at the top end since their global equivalence ratios are close to unity.

The discussion about various metrics for the inert mixing behaviors in this Sub-section may be able to provide qualitative explanations for the phenomena observed in the experiments by Rankin et al. [1]. Based on the OH^* chemiluminescence presented in Fig. 5 of Ref. [1], when the reactant mass flow rates increase, the detonation wave height increases from low (corresponding to Case 4) to intermediate (Case 5) values of mass flow rates. When the mass flow rates are further increased, the heights do not increase obviously, and even multiple waves may appear. This variation of detonation heights may be directly influenced by the mixing characteristics indicated by our LES results. In addition, the measured detonation wave speeds of Cases 2, 4 and 5 are summarized in Table 2. One can see that from Cases 4, 5 to 2, the detonation wave speed increases accordingly, i.e. from 1370 m/s to 1740 m/s. However, as mentioned above, Case 2 has relatively lower mixing efficiency and RMS values of H_2 mass fraction. Based on the experimental results in Table 2, it has higher standard deviation (i.e. 80 m/s) with respect to its wave speed. Overall, stable propagation of rotating detonation wave in

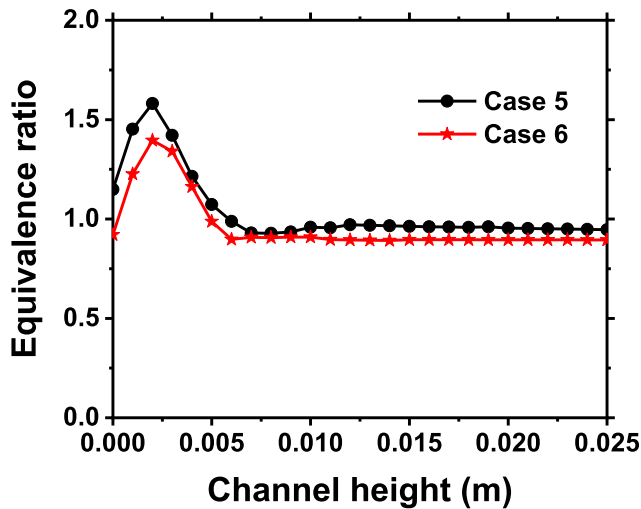


Fig. 17. Surface averaged equivalence ratio along the y-direction in Cases 5 and 6.

Table 2

The wave frequency and wave speed measurements [1] of Cases 2, 4, 5 and 6.

Cases in present simulations	Corresponding experimental cases in Ref. [1]	Wave speed (m/s)	Wave speed (% CJ)	Number of detonations waves
2	3.2.2.1	1740 ± 80	88	1
5	2.2.2.1	1700 ± 40	86	1
4	1.2.2.1	1370 ± 40	70	1
6	2.2.1.2	1480 ± 160	75	2

an RDE is not only affected by the mixing efficiency and fluctuations of H_2 mass fraction, but also by the availability of the burnable hydrogen. However, it should be acknowledged that, for accurate explanations about the detonation wave characteristics listed in Table 2, LES of reacting RDE's should be performed.

3.4. Fuel injector spacing

The effects of the fuel injector spacing on the mixing in the AFRL RDE burner are studied using a periodic burner sector with five injection orifices, as shown in Fig. 2(b). In the experiments, there are two various configurations considered, i.e. 80 and 120 orifices in total. This leads to two different azimuthal distances between two neighboring fuel orifices, i.e. 5.26 mm and 3.51 mm. They correspond to Case 6 and Case 5 in Table 1, respectively. Note that they have the same global reactant mass flow rates, but for the individual fuel injectors, fuel mass flow rate and therefore resultant fuel injection speed in Case 6 are higher than that in Case 5.

Plotted in Fig. 18 is the surface averaged RMS of H_2 mass fraction and turbulent kinetic energy in the two cases along the channel height direction. Near the fuel and air injectors, i.e. $y < 0.008$ m, the RMS of fuel mass fraction in Case 6 is higher than that in Case 5. However, for the downstream of the channel, Case 6 has the lower values. The turbulent kinetic energy is higher in Case 6 than in Case 5, due to the higher fuel injection velocity in Case 6. Similar to Fig. 14, the nominal detonability area ratios for Cases 5 and 6 are compared in Fig. 19. For most of the shown height, Case 6 has higher detonability ratio, indicating that there may have larger fraction of cross sections with detonatable compositions.

The effects of different fuel injector numbers on detonation in the

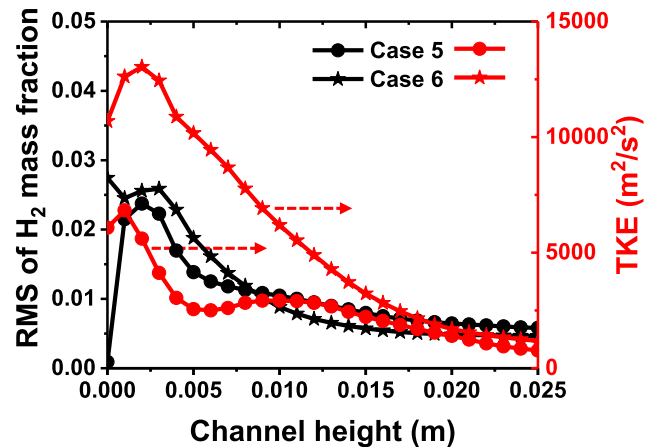


Fig. 18. Surface averaged RMS of hydrogen mass fraction in Cases 5 and 6.

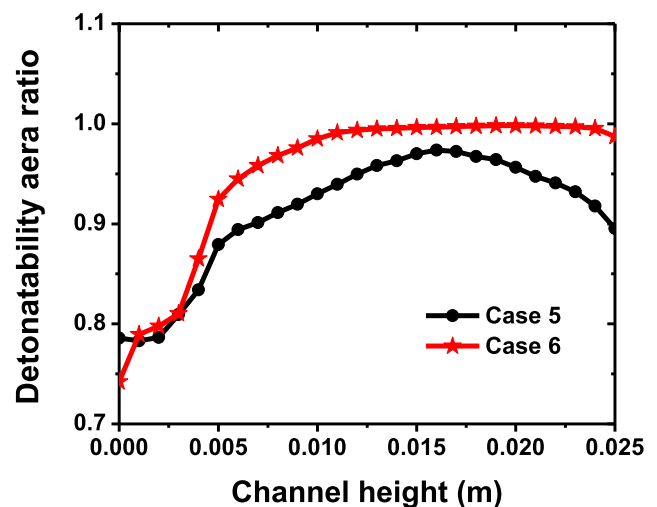


Fig. 19. Detonability area ratio along the y-direction in Cases 5 and 6.

AFRL RDE are also discussed by the experimentalists [1]. They found that in Case 6, the burner can run under two-wave mode with reduced detonation front height. This can be confirmed by the mixing characteristics indicated by our LES results.

3.5. Mixing in the full scale RDE burner

In Sub-sections 3.1–3.4, the periodic burner sector of the AFRL RDE combustor has been investigated and the corresponding aerodynamics and mixing features are discussed. It has been pointed out that there may be significant effects from three-dimensional geometry, e.g. from the curved channel walls and lateral relief of the detonation wave [1,11,19]. This implies a necessity to consider the full scale RDE combustor. Therefore, results about fuel and air mixing in three-dimensional AFRL RDE burner will be briefly analyzed in this Sub-section. This is also a preparatory step towards our future LES of rotating detonation dynamics in AFRL RDE burner.

Fig. 20 shows the distributions of resolved hydrogen mass fraction and pressure on different slices ($x = 0$ mm, $y = 0.001$ mm and $z = 0$ mm, respectively). It can be seen from Fig. 18(a) that each fuel jet exhibits different instantaneous mixing characteristics, for example the size of the fuel jet plume. The results in Fig. 18(b) also shows that the flow structures, such as the shock waves observed on the windward side

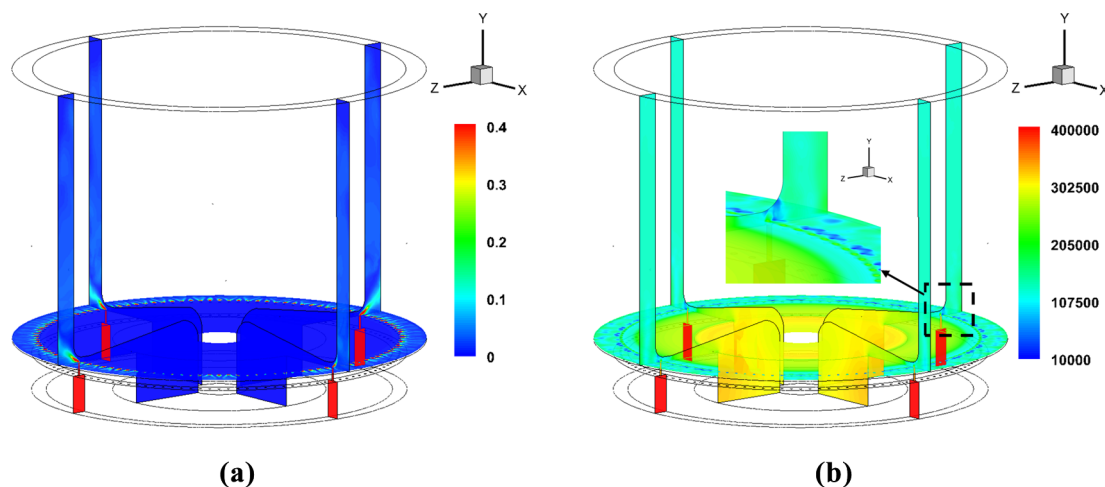


Fig. 20. Distributions of resolved (a) hydrogen mass fraction and (b) pressure of Case 9 on different slices ($x = 0$ mm, $y = 0.001$ mm and $z = 0$ mm, respectively).

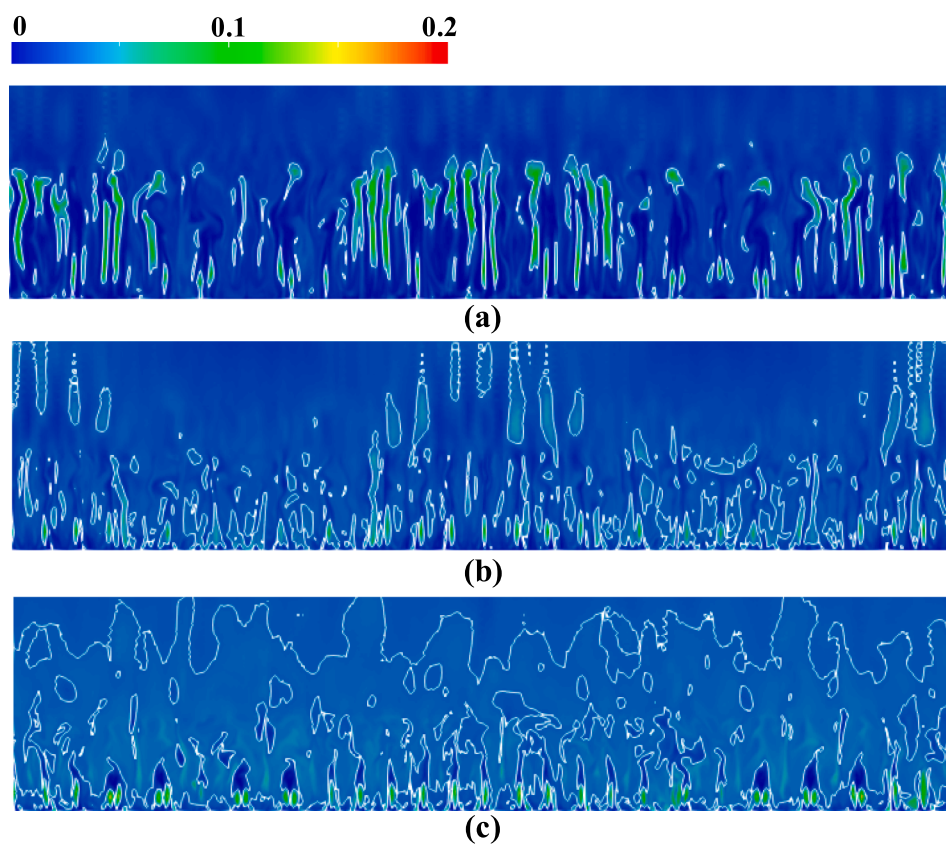


Fig. 21. Distributions of resolved hydrogen mass fraction on the unrolled annular central plane of the combustor for (a) Case 7, (b) Case 8 and (c) Case 9. The iso-lines represent stoichiometric H_2 -air composition. Images sizes are 220 mm by 35 mm.

of the fuel jet plume. These are similar to those observed in the periodic RDE burner sector with finer cells.

Moreover, distributions of resolved hydrogen mass fraction on the unrolled annular central plane of the channel with different air flow rates are shown in Fig. 21. The level of mixing can be qualitatively identified, and the mixing is mainly distributed in the near field near the top end of the combustor. It can be clearly seen that the mixing with air flow rate of 0.15 kg/s (Case 7) has poor mixing compared to larger air flow rates, i.e. 0.32 kg/s and 0.63 kg/s, in Cases 8 and 9.

the mixing near wall at the top end of the combustor (about $y < 0.003$ m) is much more uniform than that in Case 9, in which some fuel rich mixture regions with larger H_2 mass fraction are observed. These findings are consistent with the results of the mixing efficiency analysis for Cases 2, 4 and 5 with a periodic burner sector.

The comparisons of mixing efficiency and surface averaged RMS of hydrogen mass fraction between Case 2 and Case 9 are shown in Fig. 22(a) and 22(b), respectively. In addition to the slight differences, maybe related to the curved channel walls in the full case, Cases 2

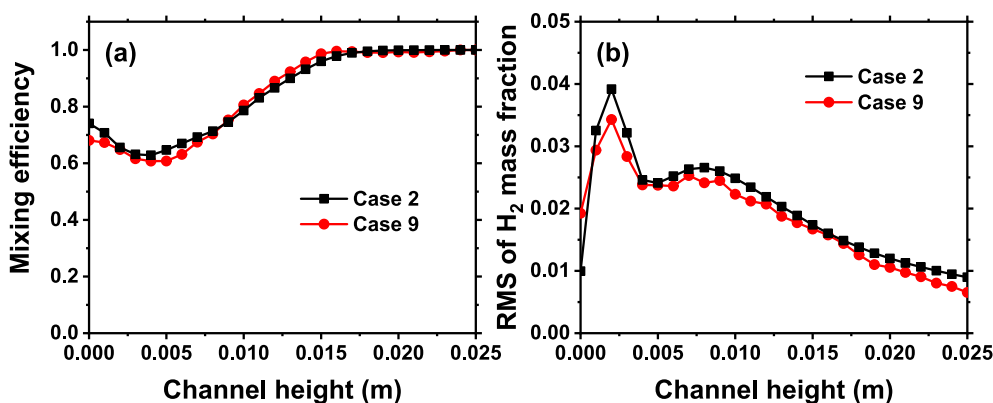


Fig. 22. (a) Mixing efficiency and (b) surface averaged RMS of hydrogen mass fraction along the y -direction in Cases 2 and 9.

(burner sector) and 9 (full annular burner) have similar results. These comparisons confirm the soundness of our above analysis based on the part of the RDE burner.

4. Conclusions

In the present work, the non-reacting flow structures and mixing characteristics in the non-premixed AFRL RDE burner [1,9] are studied with large eddy simulations to qualitatively understand the rotating detonation behaviors observed in the experiments. A series of cases have been simulated in order to explore the various physical and geometrical influences on the non-reactive flow structure and mixing, including mesh resolution, burner configuration, number of fuel injector. The primary findings from our studies can be summarized as follows.

The instantaneous vortex structures and shock wave in the non-reactive AFRL RDE are identified, and the structures are similar to those in jet in crossflow. In addition, a shock wave with different sizes and strengths at different instantaneous moment formed on the windward side of the jet plume has important influence on the mixing process near the top end of the RDE combustor. The interactions between the fuel jets and shock wave can enhance the turbulence intensity and thus promote the mixing process. Also, the compositional non-uniformity in the height and azimuthal directions are observed.

The results from quantitative analysis with five fuel injection orifices suggest that in the studied cases with various reactant flow rates, the mixing efficiency, fluctuations of H_2 mass fraction, as well as the effective mass flow rate of burnable hydrogen, demonstrate different variations along RDE height direction. For the air inflow rate of 0.32 kg/s, the mixing performance with 80 injection orifices is better than that with 120 injection orifices. The indicated tendencies provide

Appendix A.: Comparisons of sub-grid scale constants and models

In this Appendix, sensitivity to the sub-grid Schmidt number, Prandtl number and sub-grid scale model is studied using three additional cases, i.e. Case 2 with $Sc_t = 0.4$, Case 2 with $Pr_t = 0.5$ and Case 2 with one-equation sub-grid kinetic energy model [51]. Note that in the one-equation model, the sub-grid scale kinetic energy k^{sgs} is solved with transport equation. Fig. A1 shows the surface averaged RMS of hydrogen mass fraction and TKE along the y -direction for Case 2 with different sub-grid Schmidt number, Prandtl number and sub-grid scale models. It can be seen that the difference is negligible for the cases with different sub-grid Schmidt and Prandtl numbers. For the sensitivity of sub-grid model, although there are some deviations in terms of the surface averaged RMS of hydrogen mass fraction and TKE along the y -direction, the results of both WALE sub-grid model and one-equation sub-grid TKE model have the same trend and are close. The results in Fig. A1 further confirm that our LES is not affected by the choices of the sub-grid scale constants and models.

the qualitative justifications for experimental observations made by Rankin et al. [1].

Finally, the results of full scale AFRL RDE simulations are similar to those from the periodic burner sector, which is conducive to study the effects of mixing on detonation initiation and propagation in our future work on LES of AFRL RDE burner.

It should be pointed out that understanding the mixing performance in non-reacting flows from an RDE combustor would be helpful for designing or improving RDE injection nozzle and burner configuration. Meanwhile, the results from our work may also be conducive for investigations on ignition of rotating detonation waves. However, in order to study the effects of propellant mixing on rotating detonation propagation, LES of reacting cases should be conducted, which is an interesting topic for our work.

Declaration of Competing Interest

The authors declare that they have no known competing financial interests or personal relationships that could have appeared to influence the work reported in this paper.

Acknowledgements

The authors thank Professor Chiang Juay Teo and Dr Jiun-Ming Li from National University of Singapore (NUS) for helpful discussions. The simulations were performed with the computational resources from National Supercomputing Center (NSCC), Singapore. The authors thank the anonymous reviewers for the helpful comments to improve the manuscript.

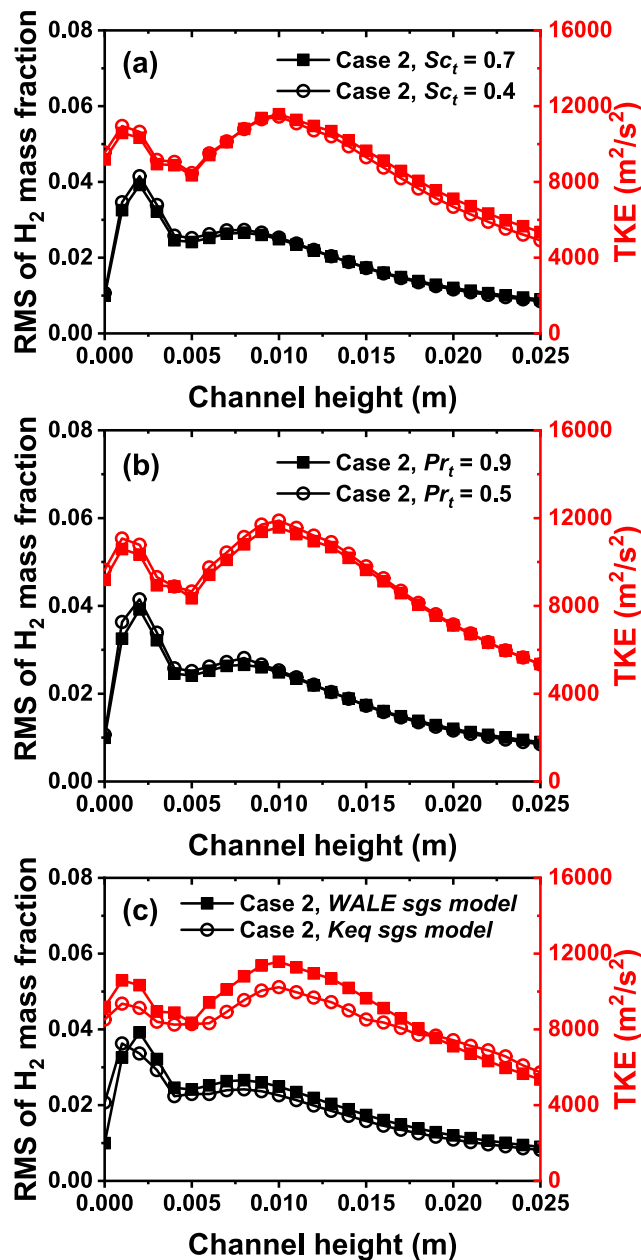


Fig. A1. Surface averaged RMS of hydrogen mass fraction and TKE along the along the y -direction for Case 2 with different sub-grid (a) Schmidt numbers, (b) Prandtl numbers and (c) LES models.

References

- [1] Rankin BA, Richardson DR, Caswell AW, Naples AG, Hoke JL, Schauer FR. Chemiluminescence imaging of an optically accessible non-premixed rotating detonation engine. *Combust Flame* 2017;176:12–22.
- [2] Nejaamtheen MN, Kim J-M, Choi J-Y. Review on the research progresses in rotating detonation engine. *Detonation Control Propuls* 2018:109–59.
- [3] Li J-M, Teo CJ, Khoo BC, Wang J-P, Wang C. *Detonation control for propulsion: pulse detonation and rotating detonation engines*. Springer; 2017.
- [4] Ji Z, Zhang H, Wang B. Performance analysis of dual-duct rotating detonation aero-turbine engine. *Aerosp Sci Technol* 2019;92:806–19.
- [5] Lu FKEMB. Rotating detonation wave propulsion: experimental challenges, modeling, and engine concepts. *J Propuls Power* 2014;4:464–70.
- [6] St. George AC, Driscoll RB, Anand V, Munday DE, Gutmark EJ. Fuel blending as a means to achieve initiation in a rotating detonation engine. 53rd. *AIAA Aerosp Sci Meet* 2015:633.
- [7] Anand V, Gutmark E. Rotating detonation combustors and their similarities to rocket instabilities. *Prog Energy Combust Sci* 2019;73:182–234.
- [8] Meyer SJ, Polanka MD, Schauer FR, Hoke JL. Parameter impact on heat flux in a rotating detonation engine. 2018 *AIAA Aerosp. Sci Meet* 2018:0400.
- [9] Rankin BA, Richardson DR, Caswell AW, Naples A, Hoke J, Schauer F. Imaging of OH* chemiluminescence in an optically accessible nonpremixed rotating detonation Engine. 53rd *AIAA Aerosp Sci Meet*. 2015. p. 1604.
- [10] Rankin BA, Fugger CA, Richardson DR, Cho KY, Hoke J, Caswell AW, et al. Evaluation of mixing processes in a non-premixed rotating detonation engine using acetone PLIF. 54th *AIAA Aerosp Sci Meet*. 2016. p. 1198.
- [11] Katta VR, Cho KY, Hoke JL, Codoni JR, Schauer FR, Roquemore WM. Effect of increasing channel width on the structure of rotating detonation wave. *Proc Combust Inst* 2018;37:3575–83.
- [12] Codoni JR, Cho KY, Hoke JL, Rankin BA, Schauer FR. Simultaneous mid-IR H₂O/CO₂ emission and OH chemiluminescence measurements within a RDE operating with and without backpressure. 2018 *AIAA Aerosp Sci Meet* 2018:1882.
- [13] Fotia M, Hoke J, Schauer F. Experimental ignition characteristics of a rotating detonation engine under backpressured conditions. 53rd. *AIAA Aerosp Sci Meet* 2015:0632.
- [14] Li J-M, Chang P-H, Li L, Yang Y, Teo CJ, Khoo BC. Investigation of injection strategy for liquid-fuel rotating detonation engine. 2018. *AIAA Aerosp Sci Meet* 2018:403.
- [15] Deng L, Ma H, Liu X, Zhou C. Secondary shock wave in rotating detonation combustor. *Aerosp Sci Technol* 2019;95:105517.
- [16] Xia Z, Ma H, Zhuo C, Zhou C. Propagation process of H₂/air rotating detonation

- wave and influence factors in plane-radial structure. *Int J Hydrogen Energy* 2018;43:4609–22.
- [17] Meng Q, Zhao N, Zheng H, Yang J. Numerical investigation of the effect of inlet mass flow rates on H₂/air non-premixed rotating detonation wave. *Int J Hydrogen Energy* 2018;43:13618–31.
- [18] Cocks PA, Holley AT, Rankin BA. High fidelity simulations of a non-premixed rotating detonation engine. 54th. *AIAA Aerosp Sci Meet* 2016:0125.
- [19] Sato T, Voelkel S, Raman V. Detailed chemical kinetics based simulation of detonation-containing flows. *ASME Turbo Expo 2018 Turbomach. Tech. Conf. Expo., American Society of Mechanical Engineers* 2018; p. V04AT04A063-V04AT04A063.
- [20] Zhao M, Zhang H. Origin and chaotic propagation of multiple rotating detonation waves in hydrogen/air mixtures. *Fuel* 2020;275:117986.
- [21] Sato T, Raman V. Hydrocarbon fuel effects on non-premixed rotating detonation engine performance. *AIAA Scitech 2019 Forum* 2019; p. 2023.
- [22] Pitsch H. Large-eddy simulation of turbulent combustion. *Annu Rev Fluid Mech* 2006;38:453–82.
- [23] Gaillard T, Davidenko D, Dupoirieux F. Numerical optimisation in non reacting conditions of the injector geometry for a continuous detonation wave rocket engine. *Acta Astronaut* 2015;111:334–44.
- [24] Gaillard T, Davidenko D, Dupoirieux F. Numerical simulation of a rotating detonation with a realistic injector designed for separate supply of gaseous hydrogen and oxygen. *Acta Astronaut* 2017;141:64–78.
- [25] Poling BE, Prausnitz JM, O'Connell JP. *The properties of gases and liquids* 5. New York: McGraw-hill; 2001.
- [26] McBride BJ. Coefficients for calculating thermodynamic and transport properties of individual species. National Aeronautics and Space Administration, Office of Management, Scientific and Technical Information. *Program* 1993;vol:4513.
- [27] Nicoud F, Ducros F. Subgrid-scale stress modelling based on the square of the velocity gradient tensor. *Flow, Turbul Combust* 1999;62:183–200.
- [28] Ben-Nasr O, Hadjadj A, Chaudhuri A, Shadloo MS. Assessment of subgrid-scale modeling for large-eddy simulation of a spatially-evolving compressible turbulent boundary layer. *Comput Fluids* 2017;151:144–58.
- [29] Otero-Pérez JJ, Sandberg RD. Compressibility and variable inertia effects on heat transfer in turbulent impinging jets. *J Fluid Mech* 2020;887.
- [30] Greenshields CJ, Weller HG, Gasparini L, Reese JM. Implementation of semi-discrete, non-staggered central schemes in a colocated, polyhedral, finite volume framework, for high-speed viscous flows. *Int J Numer Methods Fluids* 2010;63:1–21.
- [31] Kurganov A, Noelle S, Petrova G. Semidiscrete central-upwind schemes for hyperbolic conservation laws and hamilton-jacobi equations. *SIAM J Sci Comput* 2001;23:707–40.
- [32] van Leer B. Towards the ultimate conservative difference scheme. II. Monotonicity and conservation combined in a second-order scheme. *J Comput Phys* 1974;14:361–70.
- [33] Zhao M, Zhang H. Large eddy simulation of turbulent combustion and its application in detonative propulsion. Technical Report, Temasek Laboratories. Singapore: National University of; 2018.
- [34] Zhao M, Bian Y, Li Q, Ye T. Large eddy simulation of transverse single/double jet in supersonic crossflow. *Aerosp Sci Technol* 2019;89:31–45.
- [35] Huang Z, Zhang H. Numerical investigations of mixed supersonic and subsonic combustion modes in a model combustor. *Int J Hydrogen Energy* 2020;45:1045–60.
- [36] Huang Z, Zhao M, Zhang H. Modelling n-heptane dilute spray flames in a model supersonic combustor fueled by hydrogen. *Fuel* 2020;264:116809.
- [37] Huang Z, Zhang H. Investigations of autoignition and propagation of supersonic ethylene flames stabilized by a cavity. *Appl Energy* 2020;265:114795.
- [38] Zhao M, Li J-M, Teo CJ, Khoo BC, Zhang H. Effects of variable total pressures on instability and extinction of rotating detonation combustion. *Flow, Turbul Combust* 2020;104:261–90.
- [39] <http://openfoam.org> [online]. 2018.
- [40] Bluemner R, Bohon MD, Paschereit CO, Gutmark EJ. Experimental study of reactant mixing in model rotating detonation combustor geometries. *Flow, Turbul Combust* 2019;102:255–77.
- [41] Jeong J, Hussain F. On the identification of a vortex. *J Fluid Mech* 1995;285:69–94.
- [42] Mahesh K. The Interaction of jets with crossflow. *Annu Rev Fluid Mech* 2013;45:379–407.
- [43] Génin F, Menon S. Computers & Fluids Studies of shock/turbulent shear layer interaction using Large-Eddy Simulation. *Comput Fluids* 2010;39:800–19.
- [44] Yu-shan Z, Chao W, Yu-hui W, Le Jia-ling. Numerical study of mixing and flow field characteristics on a three-dimensional non-premixed rotating detonation. *J Propuls Technol* 2019;40:407–15.
- [45] Fujii J, Kumazawa Y, Matsuo A, Nakagami S, Matsuoka K, Kasahara J. Numerical investigation on detonation velocity in rotating detonation engine chamber. *Proc Combust Inst* 2017;36:2665–72.
- [46] Mi X, Higgins AJ, Ng HD, Kiyanda CB, Nikiforakis N. Propagation of gaseous detonation waves in a spatially inhomogeneous reactive medium. *Phys Rev Fluids* 2017;2:53201.
- [47] Han W, Wang C, Law CK. Role of transversal concentration gradient in detonation propagation. *J Fluid Mech* 2019;865:602–49.
- [48] Cai Z, Sun M, Wang Z, Bai X-S. Effect of cavity geometry on fuel transport and mixing processes in a scramjet combustor. *Aerosp Sci Technol* 2018;80:309–14.
- [49] Browne S, Ziegler J, Shepherd JE. *Shock and detonation toolbox*. CA: GALCIT-Explosion Dyn Lab Pasadena; 2008.
- [50] Choi J-Y, Jeung I-S, Yoon Y. Computational fluid dynamics algorithms for unsteady shock-induced combustion, Part 2: comparison. *AIAA J* 2000;38:1188–95.
- [51] Yoshizawa A. Statistical theory for compressible turbulent shear flows, with the application to subgrid modeling. *Phys Fluids* 1986;29:2152–64.